CrossMark

Effect of chromium element on transformation, mechanical and corrosion behavior of thermomechanically induced Cu–Al–Ni shape-memory alloys

M. Zare[1,2] · M. Ketabchi[1]

Abstract Cu–Al–Ni shape-memory alloys are considered as high potential materials for high-temperature applications. The aim of this research was to evaluate the increasing strain value and Cr addition on martensite morphology, transformation temperatures, mechanical, and corrosion properties of Cu–Al–Ni alloy. To this purpose, thermomechanical treatment which includes successive hot rolling, annealing, and hydraulic pressing passes was applied. In addition, tensile test, differential scanning calorimetry, and potentiodynamic polarization were carried out to compare the properties of prepared samples. The results showed that by increasing the applied strain, morphological transition from wide laths to acicular martensite with monoclinic structure was occurred. The chromium element acts as a grain refiner in this alloy by restricting the grain growth. This element leads to microstructural embrittlement, diminishing the mechanical properties. Besides, the influence of applied strain and Cr content on corrosion resistance of Cu–Al–Ni alloy was reciprocal. Despite suitable effect of Cr on corrosion behavior, increasing the applied strain facilitated the corrosion rate. Another subtle point is that both Cr addition and higher strain value reduce austenite to martensite transformation temperatures and hysteresis temperature interval.

Introduction

Shape-memory alloys (SMAs) categorize as a subset of functional, smart materials with the unique characteristic of memorizing the shape they had before pseudo-plastic deformation [1–3]. Shape-memory effects and superelasticity which are both generated by the crystallographically reversible martensitic phase transformation are significant properties of SMAs [4]. These smart materials have been widely considered in the last decade for their applications as functional materials [3, 5, 6]. Due to these extraordinary characteristics, SMAs have attracted considerable attention as materials for medical devices, sensors, and actuators [5–7]. However, in spite of the large number of studied SMAs, only two families have been investigated for industrial applications: the Ni–Ti and the Cu–Al–Ni alloys [8].

There has been a major inclination to research on single and polycrystalline Cu-based SMAs mainly due to their low cost, reasonable shape-memory effect, and relative ease of processing [5, 6, 9]. Since the Cu–Al–Ni alloys have better thermal stability compared with other Cu-based SMAs, they can be used at higher temperatures [9–11]. Cu–Al–Ni SMAs are being ameliorated as alternative functional intermetallics because of their possible use at temperatures near 200 °C in advantage over Cu–Zn–Al and Ni–Ti alloys whose maximum working temperature is 100 °C [10]. In addition, they have some other considerable advantageous rather than Ni–Ti SMAs, e.g., straightforward melting process, accurate control on casting and chemical composition, higher work/cost ratio, and perhaps most importantly better stability

✉ M. Zare
zare@aut.ac.ir

[1] Department of Mining and Metallurgical Engineering, Amirkabir University of Technology (AUT) (Tehran Polytechnic), PO Box 15875-4413, Tehran, Iran

[2] Department of Mechanical Engineering, Amirkabir University of Technology (AUT) (Tehran Polytechnic), PO Box 15875-4413, Tehran, Iran

of the two-way shape memory [12–14]. Furthermore, additional privilege can be obtained via rapid solidification, such as more stability of mechanical properties at elevated temperatures, lower rate of grain coarsening during heat treatment, proper aging resistance, and enhanced electrical and magnetic properties [15, 16].

However, Cu–Al–Ni SMAs have some restrictions for industrial applications due to their low thermal stability, brittleness, and unconvincing mechanical strength rather than other advanced materials [17]. They suffer from martensite stabilization and consequently lose the thermoelastic properties. On the other hand, the practical operation of the Cu–Al–Ni alloys is confined to those requiring very small shape changes due to their poor workability and susceptibility to brittle intergranular crack propagation [5, 18]. This is mainly because most Cu-based SMAs are sufficiently ductile when they fabricate in single crystalline forms, and polycrystals of these SMAs are brittle and are prone to intergranular fracture during martensitic transformation [19–21]. As a result, large recoverable superelasticity or shape-memory strains are rarely exhibited in bulk polycrystalline Cu-based SMAs [21]. Hence, improving the mechanical properties is an important aim for these alloys. Until now, research has demonstrated that the mechanical properties of the Cu–Al–Ni alloys can be improved by adding alloying elements coupled with heat treatment [22].

It is worth mentioning that the corrosion behavior of Cu-based binary and ternary alloys has been evaluated by some authors [23, 24]. According to their research, the addition of aluminum element to Cu-based alloys is effective in order to ameliorate the corrosion resistance when these alloys are exposed to a sulfide-containing atmosphere or high-temperature environments [23, 24]. Besides, some research reported that grain boundaries of Cu–Be alloys were preferentially attacked in the first stage of the two-stage process of stress corrosion [25–27]. However, the reports on the corrosion behavior of Cu–Al-based SMAs, especially Cu–Al–Ni SMAs, are very few [26, 27]. Thus, focusing on corrosion properties of these SMAs can be very important in order to initiate more studies in this field.

With these aims, the effect of chromium addition on martensite structure, transformation temperatures, mechanical, and corrosion behavior of Cu–Al–Ni SMAs is studied for the first time. To this purpose, thermomechanical treatment that contains successive hot rolling, annealing, and hydraulic pressing passes was applied. Specimens A–D were prepared from thermomechanically treated samples which showed perfect reversibility and shape-memory effect. Furthermore, tensile test, differential scanning calorimetry, and potentiodynamic polarization were performed to compare the properties of these specimens.

Experimental

Melting and alloying process

To carry out this work, the alloy was fabricated by smelting raw copper (Cu ≥99.9 mass%), aluminum (Al ≥99.9 mass%), and nickel (Ni ≥99.9 mass%). These elements with mass ratio presented in Table 1 were melted in induction furnace set on 1200 °C temperature and 5000–6000 Hz frequency. The accuracy of mass percentage reported by Thermo Noran energy dispersive spectroscopy (EDS) was ±0.05. In order to preclude heat loss and elements oxidation, silicon powder was used to cover the surface of melt kept in silicon carbide crucible. To produce each Cu–Al–Ni billet, 1 kg of the molten metal was poured into a permanent mold followed by quenching in ice water. Quenching process was carried out in order to prevent grain coarsening during solidification. Among five cast billets (with dimension of 197.1 × 133 × 20 mm), three of them with chromium element were used to investigate the corrosion behavior of Cu–Al–Ni SMAs. Regarding inhomogeneity of cast structure, billets were heated at 950 °C for 8 h to dissolve secondary phases and to attain homogenous β-phase. After homogenizing, samples were quenched in 25 °C water and were cut to 20 × 20.7 × 21.1 mm specimens.

Casting in induction furnace without vacuum condition leads to the variation of the chemical composition compared with its initial mass ratio. Thus, EDS was carried out to assess the finalized chemical composition. Mass percentage of elements with accuracy of ±0.05 mass% is shown in Table 2.

Thermomechanical treatment

After the initial annealing at 850 °C for 30 min, samples were pressed and annealed successively. Hydraulic pressing was performed through the direction of dendrites growth to reduce the effect of solidification defects. Ten times of pressing were applied by increasing vertical load value of 120 N per pass. Height reduction in each of the

Table 1 Chemical composition of cast ingots

Alloy no.	Elements/mass%			
	Cu	Al	Ni	Cr
1	82.0	13.0	4.0	1.0
2	85.0	10.9	3.1	1.0
3	83.5	13.0	3.0	0.5
4	84.4	12.0	3.6	–
5	83.5	13.4	3.1	–

Table 2 Chemical composition of prepared samples measured by EDS analysis

Alloy no.	Elements/mass%			
	Cu	Al	Ni	Cr
1	82.32	12.07	4.86	0.75
2	86.27	9.28	3.67	0.78
3	85.83	10.31	3.48	0.38
4	86.34	10.23	3.43	–
5	85.86	10.47	3.67	–

passes was nearly 0.7 mm. At the final step, the applied load and sample height, respectively, reached to 1240 N and 13 mm. Consequently, the height reduction in all samples was determined 35 %. Between each of the two passes, annealing operation at 850 °C for 2–4 min was carried out to recrystallize cold-worked structure. After hydraulic pressing, samples were exposed to 20 passes hot rolling to achieve plate-form shape coupled with shape-memory properties. Similarly, 850 °C heating for 2–4 min was performed between hot rolling steps. The reduction value per pass was approximately 0.6 mm, and the final thickness of sheets was reached to 1.5 mm. The total strain in all samples was 88.64 %. After the last pass of rolling, hot rolled sheets were quenched in 25 °C water in order to hinder martensite and secondary phase formation.

Shape-memory effect and microstructural evaluation

Cu–Al–Ni sheets were cut to 70 × 10 × 1.5 mm ribbons in order to evaluate shape-memory effect. All samples were initially bent 20° at ambient temperature. After plastic deformation, the temperature raised to 200 °C to compare shape memorizing of ribbons. Among all fabricated Cu–Al–Ni alloys, samples three and five were selected to microstructural and mechanical analysis due to their perfect return to the initial form. They were mechanically polished and then etched for metallographic observations. Reagent that contains 2 mL $FeCl_3$ dissolved in 2 % HCl acid was used for microstructural study. The prepared surfaces were studied using Olympus BHZ optical microscope.

Tensile test

Tensile test specimens were prepared from alloys three and five which showed more shape-memory effect rather than the other fabricated alloys. While sample D was selected from alloy three, the chemical composition of test samples A, B, and C was as similar as alloy five. The ultimate thickness and strain percentage of theses specimens are given in Table 3. The tensile test was performed using an Instron 8502-type universal testing machine operated at constant strain rate of 2 mm min^{-1}. The test was carried out at room temperature until a failure, and the fracture stress–strain was determined under the tensile load. Flat thin specimens with 80 × 5 × 1.5 mm dimensions and the gauge length of 20 mm were prepared according to ASTM standard E8.

Corrosion test

A typical electrochemical three-electrode cell was adopted for corrosion tests via Autolab M101 potentiostat–galvanostat. The test was conducted at 25 °C in open air in a glass cell containing 300 mL of 3.5 % NaCl solution. Three electrodes were used for potentiodynamic polarization tests, where the reference electrode was Ag/AgCl$_{sat}$, the counter electrode was made of platinum rod, and the specimen was the working electrode. Before each experiment, the working electrode was polished mechanically using successive grades emery papers down to 2000 grit. The electrode was washed thoroughly with triply distilled water and transferred quickly to the cell. All experiments were performed at a constant scan rate of 1.0 mV s^{-1}. The anodic polarization curves of Cu–Al–Ni SMAs were obtained by sweeping a potential range from −0.2 to 0.8 V.

Thermal analysis

The martensitic transformation cycles have been determined by differential scanning calorimeter (DSC) using a TA Q100 DSC equipment. The measurement condition for thermal analysis was handled according to the ASTM F2004-05 standard for SMAs. DSC specimens with the mass of 35 mg were prepared by an electron discharge machine. Temperature interval for thermal analysis was regulated between 0 and 250 °C. The heating and cooling regime was as follows: The samples were heated to 250 °C and maintained at this temperature for 5 min. After that, they were cooled to 0 °C with the same holding time. To reveal the reversible character of this alloy, two heating–

Table 3 Value of strain during thermomechanical treatment of Cu–Al–Ni SMAs

Sample	Ultimate thickness/mm	Applied strain/%
A	0.5	96.15
B	2.0	84.61
C	4.0	69.23
D	2.0	84.61

cooling treatments were carried out with the rate of $10\ °C\ min^{-1}$ and vice versa.

Results and discussions

Shape-memory behavior of Cu–Al–Ni alloy

As shown in Fig. 1 and Table 4, despite sample two with no shape memorizing effect, samples three and five illustrate perfect reverse deformation to their normal condition. Furthermore, samples one and four show mediocre value of shape memorizing. It is worth mentioning that the shape-memory behavior is strongly depended on chemical composition. According to Cu–Al binary phase diagram at constant nickel content, integral condition to form martensitic structure will be occurred in samples which cross within β ($AlCu_4$) phase area at higher temperature [28]. In Cu–Al–Ni SMAs, increasing Ni mass percentage leads to shift the eutectic point to higher aluminum content. Consequently, to attain $\beta \leftrightarrow R18$ martensite with monoclinic structure, the Al ratio should be increased. As shown in Fig. 2, the optimum amount of aluminum element in alloys that contain 3 mass% Ni is approximately 10–15 mass%. However, some researches showed that increasing aluminum will lead to severe brittleness of Cu–Al–Ni SMAs [28].

Since the aluminum percentage of sample two is less than adequate content to form β-phase (10 mass%), α-phase stabilization will be dominant rather than β-phase. Not only does the α-phase prevent martensitic transformation and shape-memory effect, but also it rigorously embrittles the structure. In samples one and four, higher aluminum content results in stabilizing $\alpha + \beta$ two-phase area at higher temperature. In this chemical composition, secondary α-intermetallic phases hamper the complete martensitic transformation, and the shape-memory effect has been reduced consequently. In addition, the presence of high Ni and Al content in this sample makes the structure brittle.
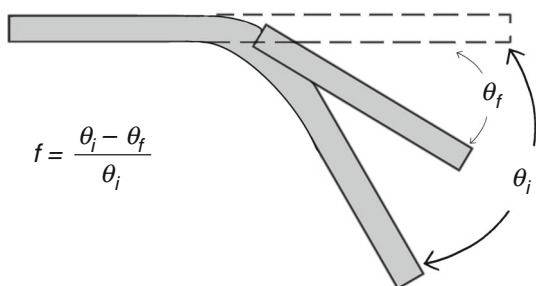

Fig. 1 Bending test parameters for expressing the degree of shape-memory effect (f: fraction of recovery, $(\theta_i - \theta_f)$: recovered bent angle, and θ_i: given bent angle)

Table 4 Shape-memory effect of prepared Cu–Al–Ni alloys

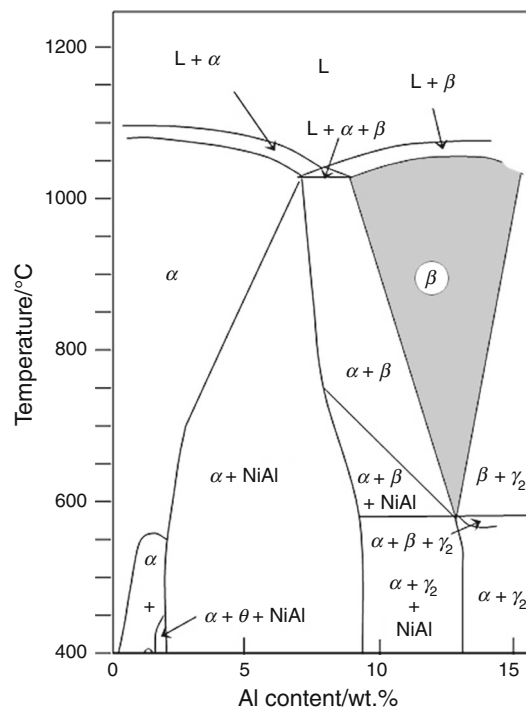| Alloy no.	1	2	3	4	5
f	0.67	0.10	0.80	0.69	0.87

Fig. 2 Vertical section of Cu–Al–Ni system at 3 mass% Ni [28]

Regarding adequate cooling rate needed to form martensite phase, $\beta \leftrightarrow$ martensite transformation is completely occurred in samples three and five due to suitable aluminum mass percentage. In inappropriate cooling rate condition, particularly at low cooling rates, decomposition of β phase to $\alpha + \gamma_2$ (Cu_9Al_4) phases at 565 °C is inevitable during solidification [8, 29]. Another subtle point is that sample three is less ductile compared with sample five due to its chromium content.

Microstructural investigation and phase analysis

The microstructural images of samples one, two, and four are demonstrated in Fig. 3. The light areas are α-phase, and the dark regions are β-phase decomposition products. In samples one and four, the partially martensitic phase with acicular morphology is referred to the presence of β-phase in $\alpha + \beta$ structure. The presence of chromium and high aluminum concentration leads to nucleate intergranular microcracks in these brittle samples. Sample two which contains light-etching proeutectoid α and lamellar eutectoid $\alpha + NiAl$ phases shows no martensite phases in its
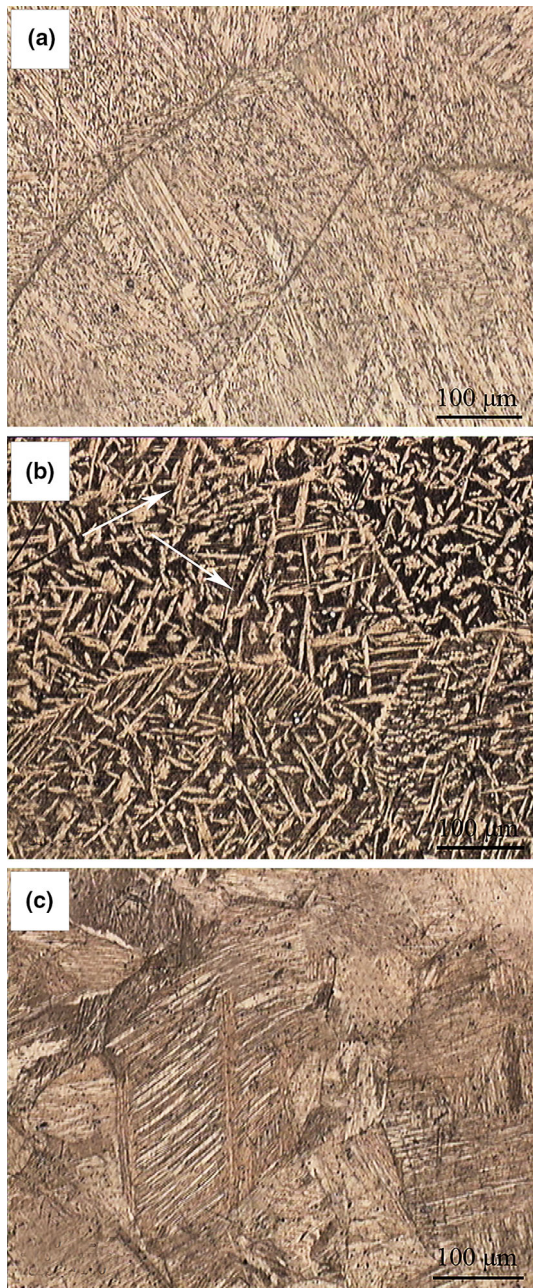
Fig. 3 Optical micrographs of samples one, two, and four: **a** sample 1, **b** sample 2, and **c** sample 4

Fig. 4 Microstructural images of samples three, and five which contain martensite laths with monoclinic structure: **a** sample 3, **b** sample 5

structure. Furthermore, β'_2 (NiAl) secondary intermetallic phases are obviously marked in this figure.

Figure 4 shows the microstructure of cast samples three and five before thermomechanical treatment. As seen, the main microstructural feature is coarse grains that contain random wide monoclinic martensite laths in some regions. The grain size in sample three is finer due to the presence of alloying elements that act as a grain refiner [15]. The chromium element has uniformly distributed into the
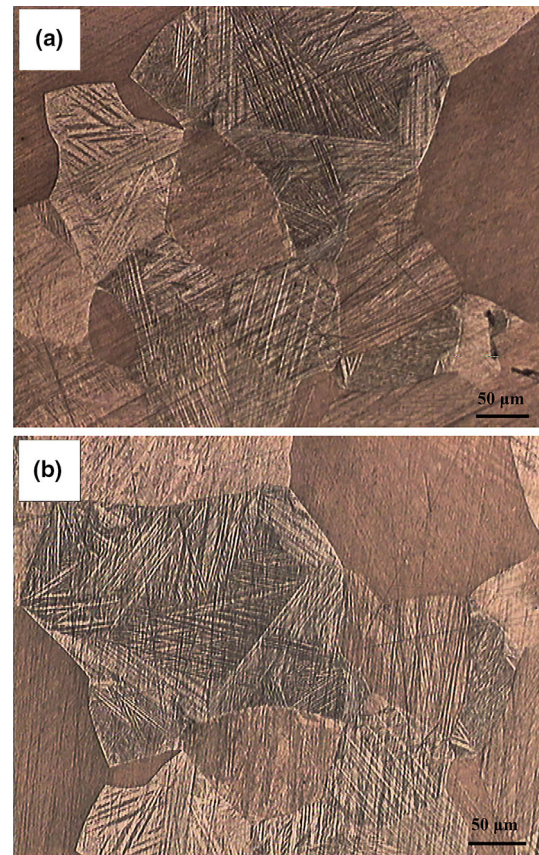
matrix, and its most effectiveness has concerned on the restriction of the grain growth.

Micrographs of specimens A, B, C, and D selected from thermomechanically treated Cu–Al–Ni SMAs are illustrated in Fig. 5. Samples B and D show needle-like martensite which contains mechanical twins. Fine needle-like martensite initiates from grain boundaries and grow to the central regions. More residual stresses that exist around grain boundaries result in generating adequate driving force needed to form martensite. In sample C exposed to low strain value, the wide martensite lath, which is within a large martensite block, has a relatively low dislocation density.

Mechanical characteristics of Cu–Al–Ni SMA

The effect of strain value and chromium element on the stress–strain curves is shown in Fig. 6. According to results given in Table 5, by increasing the ultimate thickness of specimens prepared from sample five, the tensile characteristics go initially upward and then diminish. Also, at constant strain value and chemical composition, adding Cr
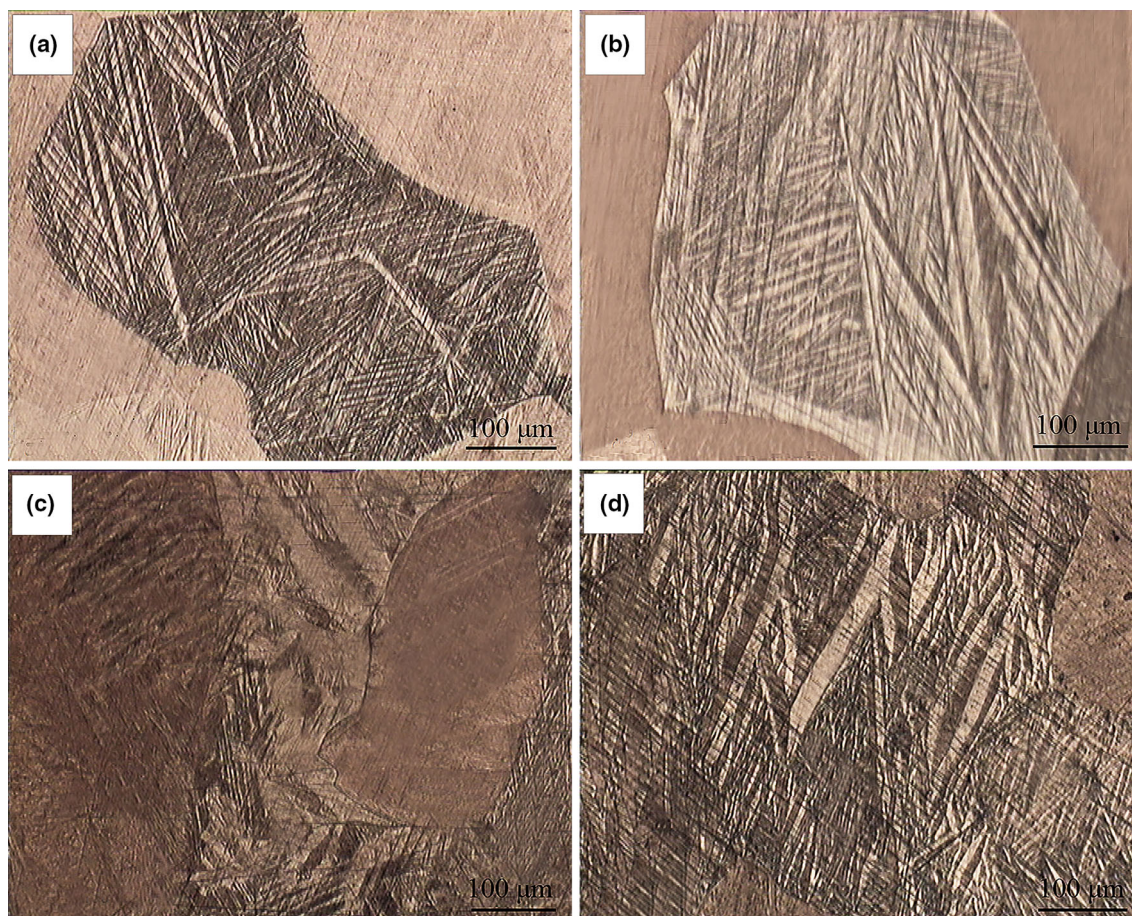
Fig. 5 Effect of Cr element and applied strain on microstructure of thermomechanically treated Cu–Al–Ni SMAs: **a** sample A, **b** sample B, **c** sample C, and **d** sample D

element leads to depress the fracture strength due to the structural embrittlement. Among all test samples, sample B shows the best tensile properties due to its perfect martensitic structure and the shape-memory behavior. After the initial elastic trend of sample A in stress–strain curve, inhomogeneous plastic deformation that contains serrated edges in parabolic zone has been occurred. This phenomenon may be referred to plastic deformation controlled by mechanical twinning process [13]. The growth of twins is responsible for abrupt decreasing the strain rate of test specimen rather than the rate of gauge movement. Despite sample A, there is no serrated edges trend in stress–strain curves of samples C and D with inhomogeneous plastic deformation. It is caused by the absence of twinning deformation in their structures.

In sample B, after elastic deformation, pseudo-plastic manner which is related to mixing variants and growth of these variants in preferential directions is the dominant mechanism. Since this specimen is brittle, the final fracture in pseudo-plastic area prevents sample to continue deforming in conventional plastic zone.
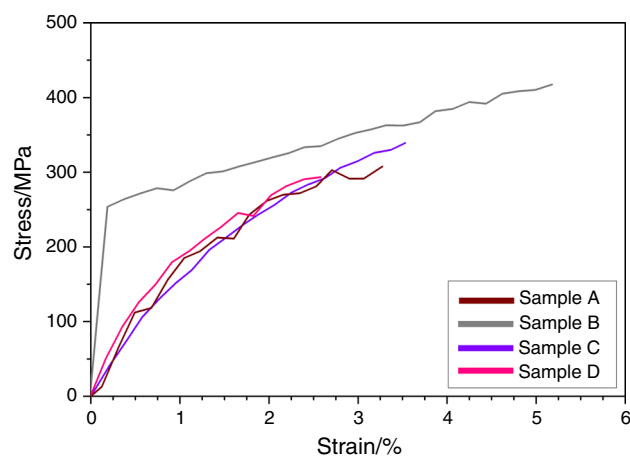

Fig. 6 Stress–strain curves of thermomechanically treated Cu–Al–Ni SMAs at different strain value and Cr content

Electrochemical measurements of Cu–Al–Ni SMA

The potentiodynamic polarization test was performed to evaluate the corrosion behavior of Cu–Al–Ni in NaCl

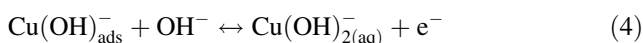**Table 5** Tensile properties of thermomechanically treated Cu–Al–Ni SMAs

Sample	Mechanical properties			
	Fracture strength/MPa	Fracture strain/%	Yield strength/MPa	Elasticity modules/MPa
A	308	3.27	112	22.32
B	417	5.17	259	135.4
C	339	3.53	152	18.5
D	293	2.60	149	26.89

solution. The voltammograms for Cu–Al–Ni alloys containing different chemical composition and strain value are recorded and presented in Fig. 7. The scan was started at −0.2 V where a transition region before active metal dissolution occurs, in which the current density stabilizes with potential. After commencing the potential scan, recording of low cathodic current started, probably due to precipitation of adsorbed species on the electrode surface, e.g., $Cu(H_2O)_{ads}$ and/or $Cu(OH)^-_{ads}$, as follows [30]:

$$Cu + H_2O \leftrightarrow Cu(H_2O)_{ads} \tag{1}$$

$$Cu + OH^- \leftrightarrow Cu(OH)^-_{ads} \tag{2}$$

The adsorption of anions on the anodized metal surface proliferates dissolution or passivation with potential enhancement. The metal attains a passive manner due to the formation of an adsorbed layer, and the adsorbed species represent a mediocre state for the active dissolution. In the region with high anodic activity, Cu atoms go into the solution as Cu^+ ions and the current density continuously ascended with potential. The increase in the anodic current can be assigned to the dissolution of an adsorbed layer via Cu^+ ion formation. The anodic peak can be attributed to dissolution/passivation process which can be categorized to below steps [31]:

Step A Dissolution, which is the dissolution of the adsorbed layer as follows:

$$Cu(H_2O)_{ads} + OH^- \leftrightarrow Cu(OH)^-_{2(aq)} + H^+ + e^- \tag{3}$$

$$Cu(OH)^-_{ads} + OH^- \leftrightarrow Cu(OH)^-_{2(aq)} + e^- \tag{4}$$

Step B Passivation, i.e., the formation of a passive film of Cu_2O according to:

$$2Cu(OH)^-_{2(aq)} \leftrightarrow Cu_2O + H_2O + 2OH^- \tag{5}$$

$$2Cu(OH)^-_{ads} \leftrightarrow Cu_2O + H_2O + 2e^- \tag{6}$$
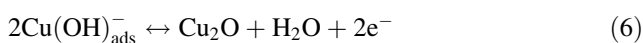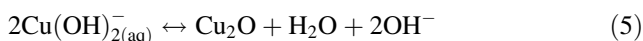
The anodic peak can be attributed to the conversion of the outer layer of the oxide film, Cu_2O, at the oxide/solution interface to Cu oxide or a hydroxide according to [31, 32]:
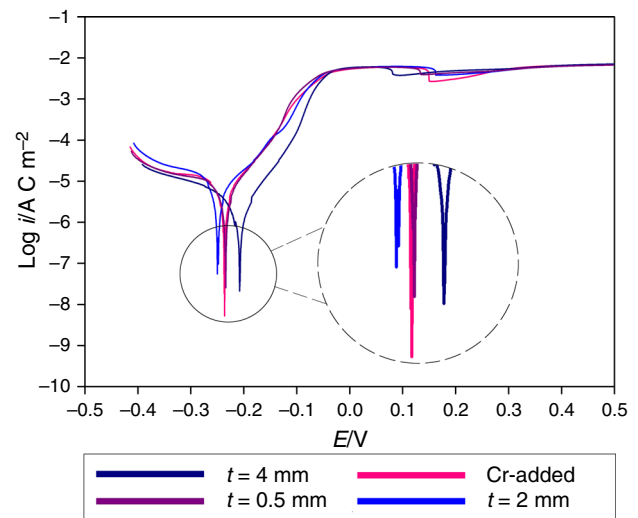
Fig. 7 Effect of Cr element and applied strain on potentiodynamic polarization curves of thermomechanically treated Cu–Al–Ni SMAs (thickness: *t*)

$$Cu_2O + H_2O \leftrightarrow 2CuO + 2H^+ + 2e^- \tag{7}$$

$$Cu_2O + 3H_2O \leftrightarrow 2Cu(OH)_2 + 2H^+ + 2e^- \tag{8}$$
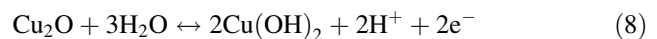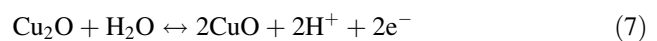
The formation of the Cu_2O layer describes the reduction of the anodic current density, which can be observed as an obvious peak. Besides, the Ni content did not have influence on the number and the position of anodic peak. This means that the kinetic process is controlled by the Cu dissolution.

The corrosion current density, corrosion rate, and polarization resistance are given in Table 6. The corrosion current density is measured after 1 h of electrode soaking in the solution. The cathodic branch of the potentiodynamic curves represents the oxygen reduction, while the anodic one illustrates Cu dissolution. In aqueous solutions, the precipitation of Cu^+ occurs during the simultaneous dissolution of the alloy and the formed Cu^+ ion undergoes further oxidation to the more stable Cu^{2+} ion as follows [30–33]:

Table 6 Corrosion properties of Cu–Al–Ni SMAs detected by potentiodynamic polarization

Sample	Corrosion properties		
	Corrosion current/A C m^{-2}	Corrosion rate/ mm year^{-1}	Polarization resistance/Ω
A	2.17E−05	0.344	2845.0
B	1.18E−05	0.187	2524.8
C	2.56E−06	0.040	7573.7
D	2.54E−05	0.402	2636.2

$$Cu \rightarrow Cu^+ + e^- \qquad (9)$$

$$Cu^+ \rightarrow Cu^{2+} + e^- \qquad (10)$$

The dissolution reaction of the Cu–Al–Ni alloys can be declared by Wharton et al. [34]: (a, b, and c are coefficients correlated with Cu, Al, and Ni elements)

$$(Cu + Al + Ni) + 0.5(a + b + c)O_2 + 2(a + b + c)H^+$$
$$\rightarrow aCu^{2+} + bAl^{3+} + cNi^{2+} + (a + b + c)H_2O \qquad (11)$$
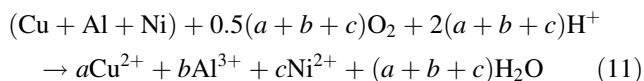
The cathodic counter part of this overall reaction is oxygen reduction which takes place in neutral solutions according to [34]:

$$0.5(a + b + c)O_2 + (a + b + c)H_2O + 2(a + b + c)e^-$$
$$\rightarrow (a + b + c)OH^- \qquad (12)$$
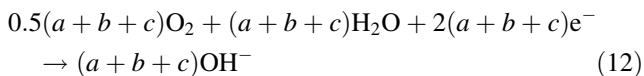
Generally, the corrosion behavior of the Cu–Al–Ni SMAs relies on the typical system of oxidation resistance materials, where Al has greater affinity toward oxygen than Cu. Under normal condition, Al_2O_3 is almost 11 times more stable than Cu_2O relative to their metals in the zero oxidation state. The higher aluminum content results in increasing the corrosion resistance due to the protective Al_2O_3 film.

According to Fig. 7 and Table 6, sample B has more negative corrosion potential compared with sample D. This indicates that at constant strain value, chromium element leads to ameliorate the polarization resistance of alloy due to formation of stable passive Cr_2O_3 oxide layer [30]. Furthermore, to discuss about the effect of martensite morphology on corrosion properties of Cu–Al–Ni SMAs, it has been concluded that sample C has higher polarization resistance than both samples A and B. In sample A, the presence of acicular martensitic structure reduces the polarization resistance intensively for two reasons. First, the acicular morphology of martensite with sharp tip leads to prepare suitable regions which contain high stress concentration. The internal stresses which cumulate adjacent to the tip and edges of needle-like martensite expedite the corrosion rate. Second, monoclinic martensite laths contain high density of dislocations and/or twins have high internal energy due to the presence of dislocations core and twining planes.

Thermal analysis results

Figure 8 shows the DSC diagrams of prepared samples. The abbreviation signs of the starting and finishing temperatures of martensite and austenite formation are considered (M_S), (M_F), (A_S), and (A_F), respectively. During heating step of all samples, evolution (A) is followed by an exothermic evolution called (B) linked to the precipitation of Al–Ni phase [14, 21, 35]. Tables 7 and 8 give the phase transformation temperatures found for the Cu–Al–Ni SMAs (with accuracy of ±0.03), revealing that the addition of chromium alters significantly the austenite ↔ martensite phase transformation temperatures: The starting and finishing transformation temperatures decrease as the Cr concentration is augmented. For the sample D, all transformation temperatures and hysteresis temperature (temperature difference between peaks of transformation during cooling and heating cycles) are low compared with the other samples. It should be noted that narrower hysteresis temperature interval presents suitable thermal properties in Cu–Al–Ni SMAs.

In addition, by comparing samples A, B, and C, it is possible to determine the effect of strain value on thermal achieved data. Sample A contains acicular martensitic structure which shows less transformations and hysteresis temperatures than samples B and C which have wide martensite lath in their microstructures. Thus, it can be resulted that by increasing the applied strain and martensite morphological transformation from wide to needle-like, both transformations and hysteresis temperatures go downward.

In order to evaluate the capability of samples to regain their initial shape (reversibility), released and possessed temperature during exothermic and endothermic transformations should be measured. To this purpose, if the difference between these two temperatures reduces, the atomic internal friction force is low, and reversible deformation will be facilitated. Thus, sample A with narrowest temperature range between two exothermic and endothermic transformations shows superior reversible deformation capability rather than the other samples.
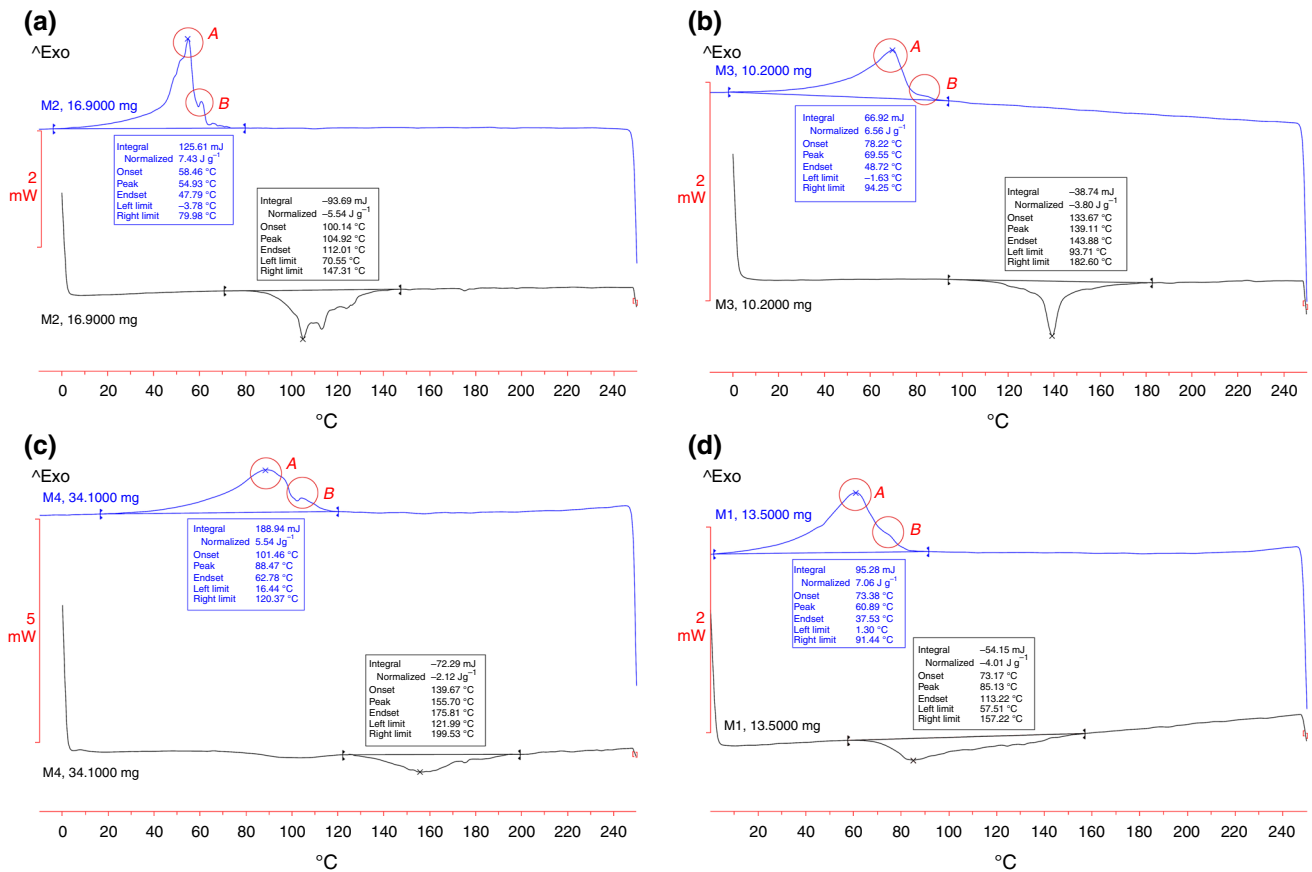
Fig. 8 DSC diagrams of thermomechanically treated Cu–Al–Ni SMAs: **a** sample A, **b** sample B, **c** sample C, and **d** sample D

Table 7 Thermal properties of Cu–Al–Ni SMAs detected by DSC analysis

Sample	Thermal properties					
	M_s/°C	M_F/°C	A_s/°C	A_F/°C	$\Delta H^{M \to A}$/J g^{-1}	$\Delta H^{A \to M}$/J g^{-1}
A	58.46	47.79	100.14	112.01	−5.54	7.43
B	78.22	48.72	133.67	143.88	−3.08	6.56
C	101.46	62.78	139.67	175.81	−2.12	5.54
D	73.38	37.53	73.17	113.22	−4.01	7.06

Table 8 Effective parameters on variation of hysteresis temperature interval

Sample	Thermal properties		
	Peak in cooling cycle, M_P/°C	Peak in heating cycle, A_P/°C	Hysteresis temperature, $A_P - M_P$/°C
A	54.93	104.92	49.99
B	69.55	139.11	69.56
C	88.47	155.70	67.23
D	60.89	85.13	24.24

Conclusions

In this study, the effect of chromium addition on transformation, mechanical, and corrosion behavior of Cu–Al–Ni SMAs is investigated for the first time. Furthermore, the different strain value during thermomechanical process of this alloy is evaluated as the other key parameter on martensite structure and transformations temperature. The main highlights can be summarized as follows:

1. The presence of chromium element, even if at low Cr concentration, embrittles the structure significantly. Thus, the tensile strength and fracture toughness will be reduced consequently.
2. Cr addition to Cu–Al–Ni SMAs results in ameliorating the corrosion properties due to the formation of stable passive Cr_2O_3 oxide layer.
3. Increasing the strain value during thermomechanical treatment leads to vary the martensite morphology from wide laths to acicular. Needle-like martensite has less corrosion resistance due to high stress concentration.
4. Increasing the applied strain decreases the starting and finishing temperatures of austenite $\leftrightarrow$ monoclinic martensite transformation. Also, the hysteresis temperature interval becomes narrower by increasing the strain value.
5. The presence of chromium is the other significant parameter on transformation temperatures. As like as strain effect, Cr additive causes to descend the transformation and hysteresis temperatures.

References

1. Karagoz Z, Aksu Canbay C. Relationship between transformation temperatures and alloying elements in Cu–Al–Ni shape memory alloys. J Therm Anal Calorim. 2013;114:1069–74.
2. Gastien R, Sade M, Lovey FC. Interaction between martensitic structure and defects in β ↔ β′ + γ′ cycling in CuAlNi single crystals. Model for the inhabitation of γ′ martensite. Acta Mater. 2008;56:1570–6.
3. Bouabdallah M, Baguenane-Benelia G, Saadi A, Cheniti H, Gachon JC, Patoor E. Precipitation sequence during ageing in β₁ phase of Cu–Al–Ni shape memory alloy. J Therm Anal Calorim. 2013;112:279–83.
4. Danoiu S, Rotaru P, Degeratu S, Rizescu S, Bizdoaca NG. Shape memory alloy-based smart module structure working under intense thermos-mechanical stress. J Therm Anal Calorim. 2014;118:1323–30.
5. Gastien R, Corbellani CE, Alvarez Villar HN, Sade M, Lovey FC. Pseudoelastic cycling in Cu–14.3Al–4.1Ni (wt%) single crystals. Mater Sci Eng A. 2003;349:191–6.
6. Gastien R, Corbellani CE, Sade M, Lovey FC. Thermal and pseudoelastic cycling in Cu–14.1Al–4.2Ni (wt%) single crystals. Acta Mater. 2005;53:1685–91.
7. Morris MA. Influence of boron additions on ductility and microstructure of shape memory Cu–Al–Ni alloys. Scr Metall Mater. 1991;25:2541–6.
8. Aksu Canbay C, Keskin A. Effects of vanadium and cadmium on transformation temperatures of Cu–Al–Mn shape memory alloy. J Therm Anal Calorim. 2014;118:1407–12.
9. Gastien R, Corbellani CE, Sade M, Lovey FC. A σ-T diagram analysis regarding the γ′ inhabitation in β ↔ β′ + γ′ cycling in CuAlNi single crystals. Scr Mater. 2006;54:1451–5.
10. Saud SN, Hamzah E, Abubakar T, Bakhsheshi-Rad HR, Zamri M, Tanemura M. Effects of Mn additions on the structure, mechanical properties, and corrosion behavior of Cu–Al–Ni shape memory alloys. J Mater Eng Perform. 2014. doi:10.1007/s11665-014-1134-1.
11. Recarte V, Perez-Landazabal JI, Rodriquez PP, Bocanegra EH, No ML, San Juan J. Thermodynamics of thermally induced martensite transformations in Cu–Al–Ni shape memory alloys. Acta Mater. 2004;52:3941–8.
12. Colic M, Rudolf R, Stamenkovic D, Anzel I, Vucevic D, Jenko M, Lazic V, Lojen G. Relationship between microstructure, cytotoxicity and corrosion properties of Cu–Al–Ni shape memory alloy. Acta Biomater. 2010;6:308–17.
13. Yildiz K, Kok M, Dagdelen F. Cobalt addition effects on martensitic transformation and microstructural properties of high-temperature Cu–Al–Fe shape-memory alloys. J Therm Anal Calorim. 2015;120:1227–32.
14. Recarte V, Perez-Landazabal JI, Ibarra A, No ML, San Juan J. High temperature β phase decomposition process in a Cu–Al–Ni shape memory alloy. Mater Sci Eng A. 2004;378:238–42.
15. Montecinos S, Cuniberti A, Romero R. Effect of grain size on the stress-temperature relationship in a β Cu–Al–Be shape memory alloy. Intermetallics. 2011;19:35–8.
16. Perez-Landazabal JI, Recarte V, Sanchez-Alarcos V, No ML, San Juan J. Study of the stability and decomposition process of the β phase in Cu–Al–Ni shape memory alloys. Mater Sci Eng A. 2006;438–440:734–7.
17. Yildiz K, Kok M. Study of martensite transformation and microstructural evolution of Cu–Al–Ni–Fe shape memory alloys. J Therm Anal Calorim. 2014;115:1509–14.
18. Recarte V, Perez-Saez RB, Bocanegra BH, No ML, San Juan J. Influence of Al and Ni concentration on the martensitic transformation in Cu–Al–Ni shape memory alloys. Metall Mater Trans A. 2002;33:2581–91.
19. Perez-Landazabal JI, Recarte V, No ML, San Juan J. Determination of the order in γ₁ intermetallic phase in Cu–Al–Ni shape memory alloy. Intermetallics. 2003;11:927–30.
20. Aksu Canbay C, Aydogdu A. Thermal analysis of Cu–14.82 wt% Al–0.4 wt% Be shape memory alloy. J Therm Anal Calorim. 2013;113:731–7.
21. Chentouf SM, Bouabdallah M, Gachon JC, Patoor E, Sari A. Microstructural and thermodynamic study of hypoeutectic Cu–Al–Ni shape memory alloys. J Alloy Compd. 2009;470:507–14.
22. Chang SH. Influence of chemical composition on the damping characteristics of Cu–Al–Ni shape memory alloys. Mater Chem Phys. 2011;125:358–63.
23. Saud SN, Hamzah E, Abubakar T, Zamri M, Tanemura M. Influence of Ti additions on the martensitic phase transformation and mechanical properties of Cu–Al–Ni shape memory alloys. J Therm Anal Calorim. 2014;118:111–22.
24. San Juan J, No ML, Schuh CA. Superelastic cycling of Cu–Al–Ni shape memory alloy micropillars. Acta Mater. 2012;60:4093–106.
25. Lovey FC, Torra V. Shape memory in Cu-based alloys: phenomenological behavior at the mesoscale level and interaction of martensitic transformation with structural defects in Cu–Zn–Al. Prog Mater Sci. 1999;44:189–289.

26. Yildiz K. Oxidation of high-temperature Cu–Al–Fe shape memory alloy. J Therm Anal Calorim. 2016;123:409–12.

27. Recarte V, Perez-Saez RB, Bocanegra EH, No ML, San Juan J. Dependence of the martensitic transformation characteristics on concentration in Cu–Al–Ni shape memory alloys. Mater Sci Eng A. 1999;273–275:380–4.

28. Sun YS, Lorimer GW, Ridley N. Microstructure and its development in Cu–Al–Ni alloys. Metall Mater Trans A. 1990;21:575–88.

29. Dagdelen F, Gokhan T, Aydogdu A, Aydogdu Y, Adiguzel O. Effects of thermal treatments on transformation behavior in shape memory Cu–Al–Ni alloys. Mater Lett. 2003;57:1079–85.

30. Badawy WA, El-Rabiee MM, Helal NH, Nady H. Effect of nickel content on the electrochemical behavior of Cu–Al–Ni alloys in chloride free neutral solutions. Electrochim Acta. 2010;56:913–8.

31. Kuo HH, Wang WH, Hsu YF, Huang CA. The corrosion behavior of Cu–Al and Cu–Al–Be shape memory alloys in 0.5 M H_2SO_4 solution. Corros Sci. 2006;48:4352–64.

32. Ismail KM, Badawy WA. Electrochemical and XPS investigations of cobalt in KOH solutions. J Appl Electrochem. 2000;30:1303–11.

33. Al-Kharafi FM, Badawy WA. Electrochemical behavior of vanadium in aqueous solutions of different pH. Electrochim Acta. 1997;42:579–86.

34. Wharton JA, Barik RC, Kear G, Wood RJK, Stokes KR, Walsh FC. The corrosion of nickel–aluminum bronze in seawater. Corros Sci. 2005;47:3336–67.

35. Bouabdallah M, Cizeron G. Caractérisation des changements de phase développés dans un alliage AMF du type Cu–Al–Ni, par dilatométrie de trempe et microcalorimétrie différentielle. Eur Phys J Appl Phys. 1998;1:163–72.